

Observed Nonmodal Growth of the Pacific–North American Teleconnection Pattern

BENJAMIN A. CASH AND SUKYOUNG LEE

Department of Meteorology, The Pennsylvania State University, University Park, Pennsylvania

(Manuscript received 26 July 1999, in final form 30 May 2000)

ABSTRACT

A linear-stochastic model is applied to the 10-day low-pass streamfunction field at 300, 500, and 850 mb for 40 winter seasons of Northern Hemisphere NCEP–NCAR reanalysis data. The linear operator is derived from the observed multilevel covariances, allowing for statistical representation of nonlinear processes. While all empirical normal modes of the system are decaying, increase in the streamfunction variance is possible through nonmodal growth. When the evolution of the streamfunction field following the optimal perturbation is predicted, the Pacific–North American teleconnection pattern (PNA) is found to be the most probable state of the atmosphere. Sixty-eight percent (70%) of positive (negative) PNA events are found to follow high projections onto the leading optimal, suggesting the PNA arises through constructive interference between the decaying modes and may be treated as a linear response to Gaussian white noise stochastic forcing. Implications for PNA timescale and onset mechanisms are also discussed.

1. Introduction

Low-frequency variability of the extratropical atmosphere, first systematically identified by Wallace and Gutzler (1981), has been the subject of numerous studies. Over the past two decades, several mechanisms have been proposed to explain the growth and maintenance of some of the dominant low-frequency teleconnections, such as the Pacific–North American teleconnection pattern (PNA), the Western Pacific teleconnection pattern (WP), and the North Atlantic oscillation (NAO). As suggested by Horel and Wallace (1981), one plausible mechanism involves a poleward-propagating Rossby wave train that has been excited by an “external” tropical heat source (Hoskins and Karoly 1981; Webster 1981). A second mechanism is barotropic (Simmons et al. 1983) or combined baroclinic/barotropic (Frederiksen 1983) instability. Feedback by high-frequency eddy vorticity flux forms the core of the third mechanism (Lau 1988; Branstator 1992; Ting and Lau 1993), which addresses the question of maintenance of the low-frequency anomalies. The existence of teleconnection-like patterns in a GCM integration that lacks SST anomalies (Lau 1981) seems to support the latter two possibilities, and implies that these patterns may be “internally” generated and maintained.

Although seemingly separate mechanisms, consid-

eration of a few points helps us to integrate the above three mechanisms into a single cohesive picture. First, the distinction between external forcing (e.g., Horel and Wallace 1981) versus internal excitation (Lau 1981) may be unwarranted. While positive SST anomalies are expected to trigger more frequent and/or stronger positive convective heating anomalies, it is also conceivable that positive heating anomalies can arise in the absence of any positive SST anomalies. For example, a reduction in static stability, rather than an increase in the SST, can also lead to enhanced convection. Therefore, it is also possible that the low-frequency anomalies found by Lau (1981) are forced by a tropical heat source. A review of some of the theories and observations given above can be found in Frederiksen and Webster (1988).

Second, the above result of Simmons et al. (1983) does not contradict the possibility that the teleconnection patterns are initiated as forced Rossby wave trains. In that study, they stress that the use of normal mode nomenclature should not be interpreted as claiming that teleconnection patterns begin as infinitesimally small amplitude perturbations undergoing exponential growth. From the perspective of a forced wave train, the mechanism proposed by Simmons et al. can be viewed as a forced Rossby wave train acquiring the appropriate form so as to further amplify by extracting energy from the background flow.

Third, the long time averaging, typically performed in diagnostic studies of teleconnection patterns, may overemphasize the role played by the high-frequency eddy fluxes. As Feldstein (1998) points out, if time averaging is performed over a period longer than the time-

Corresponding author address: Dr. Benjamin A. Cash, Geophysical Fluid Dynamics Laboratory, P. O. Box 308, Forrestal Campus, Princeton, NJ 08542.
E-mail: bac@gfdl.gov

scale of the low-frequency phenomenon, the vorticity equation takes on the following form, $0 \approx \partial \bar{\zeta} / \partial t = \bar{L} + \bar{N}$, where the overbar denotes a time mean, ζ is the vorticity, and L and N represent linear and nonlinear terms, respectively. This indicates that sufficiently long time averaging requires a balance between the linear terms, for example, relative vorticity advection of the low-frequency anomaly by the time mean flow, and nonlinear terms, for example, the divergence of the high-frequency eddy vorticity fluxes. This must be true even if the low-frequency anomaly grows and decays linearly, with the high-frequency eddy vorticity fluxes playing only a marginal role. In fact, Feldstein (2001, manuscript submitted to *Quart. J. Roy. Meteor. Soc.*, hereinafter F2001) shows that the linear terms in the vorticity equation dominate both the growth and the decay of the PNA, and that the high-frequency vorticity fluxes prolong the lifetime of the PNA by only two days.

Considering the three points raised above, a possible picture emerges that is able to integrate all the findings summarized in the first paragraph. Suppose that a low-frequency anomaly is excited by tropical heating, or perhaps by anomalous extratropical high-frequency eddies. If the anomaly takes the form of, say, the PNA, it further amplifies by extracting energy from the zonally varying background flow. As the high-frequency eddies are reorganized by the low-frequency anomaly (Branstator 1995), the high-frequency vorticity fluxes, in turn, reinforce the low-frequency flow. Despite this high-frequency eddy feedback, linear dispersion continues, and the low-frequency anomaly eventually decays.

Given the chaotic nature of the atmospheric flow, however, it is unlikely that there is a well-defined timescale for the “forcing,” whether it is a tropical heat source or high-frequency eddy vorticity fluxes. Thus, to the extent that these processes can be collectively modeled as stochastic forcing, the result of Feldstein (1998) and F2001 suggests that a linear stochastic model [see (1) below] may be adequate for describing the evolution of the low-frequency flow. Although none of the teleconnection patterns was specifically looked for, Newman et al. (1997) attempted to explore such a possibility with a linear barotropic stochastic model. They concluded that a linear barotropic model, forced with either white or red noise, is unable to explain the variance of the observed low-frequency flow. In addition, Sardeshmukh et al. (1997) found that none of the observed initial perturbations that lead to low-frequency anomalies projects strongly onto the growing barotropic optima. This cast further doubt on the linear barotropic model’s ability to successfully capture the *temporal evolution* of the observed low-frequency anomaly.

As we will show in this paper, an alternative approach is to explore the ability of a stochastic model derived from the observed flow.¹ Such a stochastic model im-

plicitly retains the statistical properties of processes such as tropical heating, baroclinicity, nonlinearity, as well as linear processes involving the observed flow. Success of the linear stochastic model can provide us with a new avenue for furthering our knowledge of low-frequency variability, and also for improving the forecast of shorter timescale phenomena. The dataset and methodology used for the analyses are described in section 2, and the results are presented in section 3. Conclusions and suggested areas of future investigation follow in section 4.

2. Data and methodology

a. Dataset

We analyze 40 winter seasons [December–January–February (DJF)] from the National Centers for Environmental Prediction–National Center for Atmospheric Research (NCEP–NCAR) reanalysis dataset for 1958–97, a detailed description of which may be found in Kalnay et al (1996). The daily vorticity field is converted to rhomboidal-15 horizontal resolution. The low-pass (>10 days) streamfunction anomalies at 300, 500, and 850 mb are then calculated, where the anomalies are relative to the smoothed calendar mean for each day, thus removing the seasonal cycle. We then obtain the empirical orthogonal functions (EOFs) by calculating the covariance matrix of the anomalies among all three levels in the Northern Hemisphere (NH). The first 40 EOFs (representing 89% of the total variance) are retained, and all subsequent calculations are performed in EOF space. Sensitivity of the results to the choice of EOFs will be discussed in section 3. The results are then transformed to gridpoint space for display. A similar set of calculations was performed on the low-pass NH 300-mb streamfunction alone, however, in this work all results are from the three level calculations unless otherwise specified.

b. Stochastic model

The following discussion closely follows Penland and Sardeshmukh (1995), and readers are referred to that work for a more detailed description. Briefly, one of the simplest possible models of a dynamical system is

$$\frac{d\mathbf{x}}{dt} = \mathbf{B}\mathbf{x} + \boldsymbol{\xi}, \quad (1)$$

where \mathbf{x} is the state vector (in this case, the vector of the time-dependent coefficients of our 40 EOFs), \mathbf{B} is a linear matrix, and $\boldsymbol{\xi}$ is a Gaussian white noise forcing. Equation (1) is a form of the Langevin equation (Gardiner 1985), and thus the most probable state of a system described by (1) at a time $t_o + \tau$ is simply

$$\mathbf{x}(t_o + \tau) = \exp(\mathbf{B}\tau)\mathbf{x}(t_o). \quad (2)$$

The linear system matrix \mathbf{B} may be determined from the statistics of the data, such that

¹ See Penland and Sardeshmukh (1995) for an application of this model to the evolution of the tropical sea surface temperatures associated with El Niño Southern Oscillation.

$$\mathbf{B} = \tau_o^{-1} \ln[\mathbf{C}(\tau_o)\mathbf{C}(0)^{-1}], \quad (3)$$

where $\mathbf{C}(0) = \langle \mathbf{x}(t)\mathbf{x}(t)^T \rangle$ and $\mathbf{C}(\tau_o) = \langle \mathbf{x}(t + \tau_o)\mathbf{x}(t)^T \rangle$ are the covariance and lagged-covariance matrices, respectively. Note that while \mathbf{B} is linear, it is derived from the statistics of the full system, and as such includes information on the statistical effects of nonlinear processes. Note also that τ in (2) and τ_o in (3) represent fundamentally different quantities. Here, τ is simply a period of time over which the system evolves, whereas τ_o is the lag chosen for calculating the covariances that determine the system matrix \mathbf{B} .

Letting $\mathbf{G}(\tau) = \exp(\mathbf{B}\tau)$, from (2), we can write the evolution of the L2 norm (variance) of the system as

$$\mathbf{x}^T(t_o + \tau)\mathbf{x}(t_o + \tau) = \mathbf{x}^T(t_o)\mathbf{G}^T(\tau)\mathbf{G}(\tau)\mathbf{x}(t_o). \quad (4)$$

If $\mathbf{x}_j(t_o) = \boldsymbol{\phi}_j(\tau)$, where $\boldsymbol{\phi}_j(\tau)$ is the j th eigenvector of $\mathbf{G}^T\mathbf{G}$, defining $E(t_o + \tau) = \mathbf{x}^T(t_o + \tau)\mathbf{x}(t_o + \tau)$ and $E(t_o) = \mathbf{x}^T(t_o)\mathbf{x}(t_o)$, (4) reduces to

$$E(t_o + \tau) = \lambda_j E(t_o), \quad (5)$$

where λ_j is the eigenvalue corresponding to the eigenvector $\boldsymbol{\phi}_j$. Thus, λ_j gives the amplification factor for E over the period τ , when the eigenvector, $\boldsymbol{\phi}_j(\tau)$, represents the corresponding initial state. Those eigenvectors with $\lambda_j > 1$ are referred to as growing optimal initial perturbations, or growing optimals. Throughout this work we will refer to $\boldsymbol{\phi}_1(\tau)$, corresponding to the largest eigenvalue λ_1 , as the leading optimal.

c. Empirical normal modes

The solutions of (1) when the forcing $\boldsymbol{\xi}$ is neglected, that is,

$$\frac{d\mathbf{x}}{dt} = \mathbf{B}\mathbf{x},$$

are referred to in the literature as both Principle Oscillation Patterns (POPs) (Hasselmann 1988), and as Empirical Normal Modes (ENMs) (Penland and Ghil 1993). These solutions take the general form $\mathbf{u}_j \exp(b_j)c_j$, where \mathbf{u}_j is the j th complex eigenvector of \mathbf{B} , b_j is the complex eigenvalue, and c_j is an arbitrary complex constant. The ENMs form a complete set, with the contribution of an individual ENM to \mathbf{x} given as

$$\mathbf{x}_j = z_j \mathbf{u}_j,$$

where $z_j = \mathbf{v}_j^T \mathbf{x}$ is a complex coefficient, and \mathbf{v}_j is the j th eigenvector of \mathbf{B}^T . Here, \mathbf{v}_j represents the adjoint of \mathbf{u}_j , forming a biorthonormal set such that

$$\mathbf{U}\mathbf{V}^T = \mathbf{U}^T\mathbf{V} = \mathbf{I},$$

where \mathbf{U} and \mathbf{V} contain the \mathbf{u}_j s and \mathbf{v}_j s, respectively, and \mathbf{I} is the identity matrix.

Table 1 lists the decay rates and periods for the 40 ENMs diagnosed for $\tau_o = 5$ days in (3). The ENMs listed as pairs correspond to complex conjugates of b_j , and single ENMs to real b_j . Repeating the ENM analysis

TABLE 1. Empirical normal modes of \mathbf{B} for $\tau_o = 5$ days.

Empirical normal modes		
Mode	Decay rate (days ⁻¹)	Period (days)
1/2	8	17
3/4	100	19
5/6	5	23
7/8	3	121
9/10	4	45
11/12	6	28
13/14	9	26
15/16	7	29
17/18	7	31
19/20	5	197
21/22	6	54
23/24	6	419
25/26	9	46
27/28	9	55
29/30	8	107
31/32	8	415
33/34	9	160
35/36	14	187
37	17	∞
38/39	20	344
40	50	∞

for larger values of τ_o (not shown) demonstrates that as τ_o increases the smallest half-period of the ENMs approaches τ_o . In order to avoid the spurious results that occur when these timescales are similar, $\tau_o = 5$ days is used for all results presented in this paper. Table 1 also shows that, as expected, all ENMs of the system are decaying. This immediately leads to the result that any growth identified through (5) must come through constructive interference of the ENMs, and not through exponentially growing instabilities.

3. Results

a. Growing optimals

The magnitude of the leading eigenvalue of $\mathbf{G}^T\mathbf{G}$ as a function of lag τ is shown in Fig. 1 for $\tau_o = 5$ days in (3). This curve, also known as the Maximum Amplification (MA) curve (Penland and Sardeshmukh 1995), indicates that for 40 EOFs, amplification of the variance of ψ' , the low-pass streamfunction anomaly, is possible over a period of 20 days, increasing from a value of 1.5 for day 1 to a maximum value of 2.7 for day 5. While we find a number of growing optimals for various time periods, here we focus only on the leading optimal. We also see in Fig. 1 that the values of the MA curve depend somewhat on the number of EOFs chosen. EOFs with smaller eigenvalues may be corrupted by sampling errors, and may unduly influence the calculation of \mathbf{B} through the matrix inversion in (3) (Zhang et al. 1997). However, for the range of 30–40 EOFs we see relatively little sensitivity. Thus, all results presented here will be for calculations using 40 EOFs, allowing us to retain the maximum amount of variance

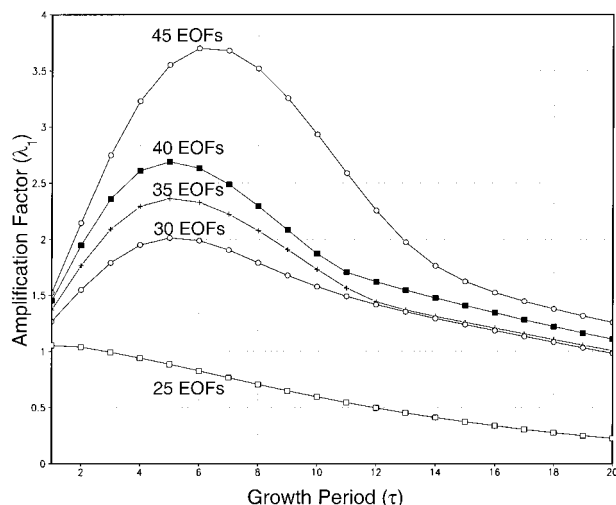


FIG. 1. Maximum amplification curve (leading eigenvalue of $\mathbf{G}^T\mathbf{G}$), for $\tau_o = 5$ days. Each curve corresponds to a separate EOF truncation.

from the original data while remaining within the robust region. We shall also see that this choice of EOFs provides the best agreement with the observations.

The structure of the leading optimal for day 5, $\phi_1(5)$, is shown in Figs. 2a–c. The leading optimal is primarily concentrated over the north Pacific. At 300 mb (Fig. 2a), a positive–negative couplet lies along the east coast of Asia, with a stronger couplet of opposite sign farther downstream. We also find a relatively weaker positive center over the tropical western Pacific. The pattern at 500 mb (Fig. 2b) is similar to that at 300 mb, with an eastward shift in the positive center over the tropical western Pacific. At 850 mb (Fig. 2c), this positive center shifts still farther eastward, while in the extratropics only the positive center in the Gulf of Alaska is present. Together, Figs. 2a–c show the leading optimal is approximately equivalent barotropic in the extratropics, and more baroclinic in the Tropics.

By applying Eq. (2) to the leading optimal shown in Figs. 2a–c, we arrive at the most probable state of the atmosphere corresponding to the maximum amplification of the ψ' variance. This state (Figs. 2d–f), obtained for $\tau = 5$ days, bears a striking resemblance to the negative phase of the PNA pattern. We find positive centers over the southeastern United States and the Gulf of Alaska at 300 mb (Fig. 2d), and negative centers over western North America and the subtropical Pacific. These centers of action compare favorably with those diagnosed in previous observational studies (Wallace and Gutzler 1981; Barnston and Livezey 1987). At 500 mb (Fig. 2e) we see a weakened version of the 300-mb pattern, consistent with the relation between Figs. 2a and 2b. At 850 mb (Fig. 2f), only a single positive center is apparent, resembling the surface footprint of the observed PNA (Wallace and Gutzler 1981).

While Fig. 2 shows a definite vertical structure to

both the leading optimal and the most probable future state, our analysis is not qualitatively dependent on the use of three levels in deriving the linear operator in (1). Figure 3 shows the same analysis as presented in Fig. 2, where we have used data at 300 mb only, and 35 EOFs (89% variance). The maximum growth now takes place over 6 days. The similarity between Figs. 2a and 3a and Figs. 2d and 3b demonstrates that sufficient information is present in the statistics of the 300-mb flow to capture the leading optimal and its subsequent evolution.

b. Verification of PNA

While section 3a shows that patterns resembling the PNA evolve from the leading optimal, it is important to show that Figs. 2d–f and 3b do truly capture the PNA. Even significant shifts in the phase of the wave pattern can be difficult to detect by eye. To quantitatively compare our pattern with the conventional PNA, we first calculate daily values of the projection of the observed low-frequency ψ' field onto the pattern in Figs. 2d–f, such that

$$\alpha(t) = \sum_{ijk} \psi'_{ijk} P_{ijk} \cos(\theta_j),$$

where $\alpha(t)$ is the value of the projection, i and j are the NH longitude and latitude, respectively, k our three pressure levels, P_{ijk} is the value of our pattern at each grid-point, and θ_j is the latitude. We then take monthly averages of α , and compare these values to the Barnston and Livezey (1987) PNA index for the same months, available from the Climate Prediction Center (CPC). The comparison between the two indices is shown in Fig. 4. Despite the numerous differences in the method of calculation between these two indices (the CPC index is derived from the rotated principal components of the 700-mb monthly mean geopotential height anomalies), they show remarkable agreement. The two series correlate at 0.77, and an examination of the series themselves shows close correspondence in the placement of the peaks and valleys, indicating that the pattern identified in section 3a is indeed the PNA.

Having determined that Figs. 2d–f show the PNA, we now turn to the link between the PNA and our leading optimal. While the PNA is the most probable state of the atmosphere following a perturbation of the form shown in Figs. 2a–c, it is not clear that this relationship will be observed in the real atmosphere. For example, Sardeshmukh et al. (1997) show that the observed flow seldom projects onto the growing optimals in their barotropic model. To examine the relationship between the leading optimal and the PNA in the observed data, we calculate

$$\beta(t) = \sum_{ijk} \psi'_{ijk} \phi_{1ijk}(5) \cos(\theta_j),$$

where $\beta(t)$ is the projection of ψ' onto the leading op-

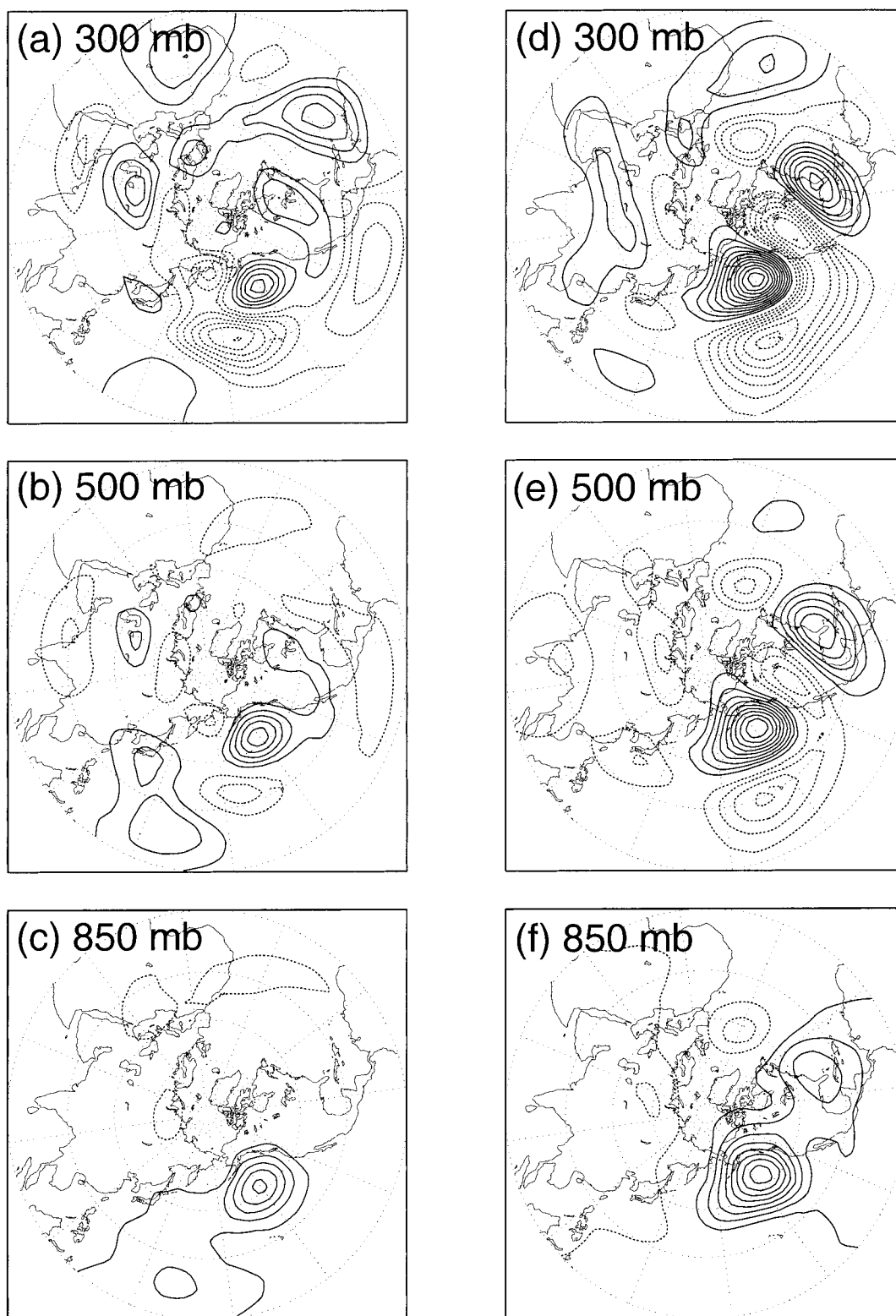


FIG. 2. Left: Leading eigenvector ϕ_1 of $\mathbf{G}^T \mathbf{G}$ for $\tau_o = 5$ days, and 40 EOFs at (a) 300, (b) 500, and (c) 850 mb. Right: $\mathbf{G}(\tau)\phi_1(\tau)$ for $\tau = 5$ days at (d) 300, (e) 500, and (f) 850 mb. Contour interval is 0.15, solid contours are positive, dashed contours are negative, and the zero contour is omitted.

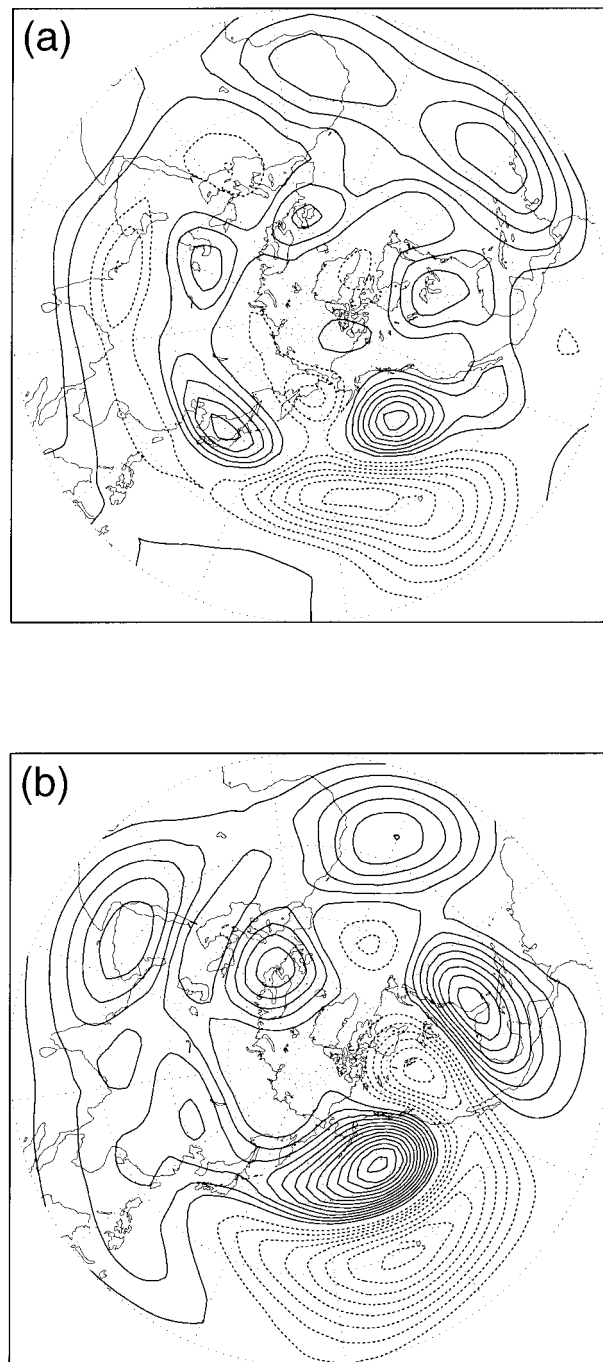


FIG. 3. As (a) Fig. 2a and (b) Fig. 2d, except that only 300-mb data are used, the first 35 EOFs are included, and τ is 6 days.

timal. The two series, $\alpha(t)$ and $\beta(t)$, are then normalized by their respective standard deviations and shown in Fig. 5 for a segment of the dataset. In general, we see high values of α are preceded by high values of β . Quantitatively, if we define $|\alpha| > 1$ as a PNA event, we find that 68% (70%) of all positive (negative) PNA events follow $\beta < -1$ ($\beta > 1$) within 7 days.

By performing lag composites on the highest $\beta > 1$ prior to a negative PNA event, we see that the ψ' field at lag 0 (Fig. 6a) strongly resembles the leading optimal (compare with Fig. 2a) at 300 mb. As the event progresses (Figs. 6b–e) we see the upstream centers weaken and eventually disappear, while downstream development takes place over the North American continent. By lag +5 (Fig. 6f), we see the fully developed PNA pattern, which closely resembles the PNA pattern derived from the optimal growth analysis (see Fig. 2f), again confirming that the majority of PNA events follow high projections onto the leading optimal. A timescale of 5 days for PNA growth is consistent with that found by Dole and Black (1990) for their persistent anomalies. Composites of ψ' for those $|\beta| > 1$ not followed by a PNA event as defined above, that is, $|\alpha| > 1$, still show a distinct, but smaller amplitude, PNA pattern (not shown), indicating that the lack of a PNA event is a function of our event criteria, and not because the PNA pattern was not present.

Given that the majority of the observed PNA events follow high projections of the flow onto the leading optimal, we can also compare the observed amplification of the ψ' variance with the values derived from the MA curve (Fig. 1), by calculating

$$\gamma(t_i) = \frac{\bar{\mathbf{x}}^T(t_i + \tau)\bar{\mathbf{x}}(t_i + \tau)}{\bar{\mathbf{x}}^T(t_i)\bar{\mathbf{x}}(t_i)},$$

where $\gamma(t_i)$ is the composite observed amplification factor as a function of lag t_i , where $t_i = 0$ corresponds to the time of the local maximum in $|\beta|$, provided $|\beta| > 1$, $\tau = 5$ days is the growth period, and $\bar{\mathbf{x}}$ is the composite state vector. Figure 7 shows $\gamma(t_i)$ for both positive and negative PNA events. Although there appears to be a systematic difference between the positive and negative PNA events, comparison of the maximum values with those from the MA curve (Fig. 1) shows good agreement; the average maximum observed amplification at 5 days, for 40 EOFs, between the positive and negative phase events is 2.75, which agrees closely with the MA value of 2.7. This result further supports the hypothesis that Figs. 2 and 5 represent the behavior of the PNA in the real atmosphere.

Figure 7 also demonstrates that the observed amplification is relatively insensitive to the choice in the number of retained EOFs in the range of 30–40. For the calculations made at 300 mb only (not shown), we see similar values of observed amplification. However, for this single-level calculation, the amplification factor from the MA curves, that is, the value of λ_1 , are consistently lower than the observed amplification. For example, using 35 EOFs, the MA curve indicates a maximum amplification of 2.15, while the observed average is 3.15. Thus, it appears that while the data at 300 mb alone contain sufficient information to reproduce the spatial evolution of the leading optimal of the multilevel calculation, it cannot as accurately predict the observed amplification.

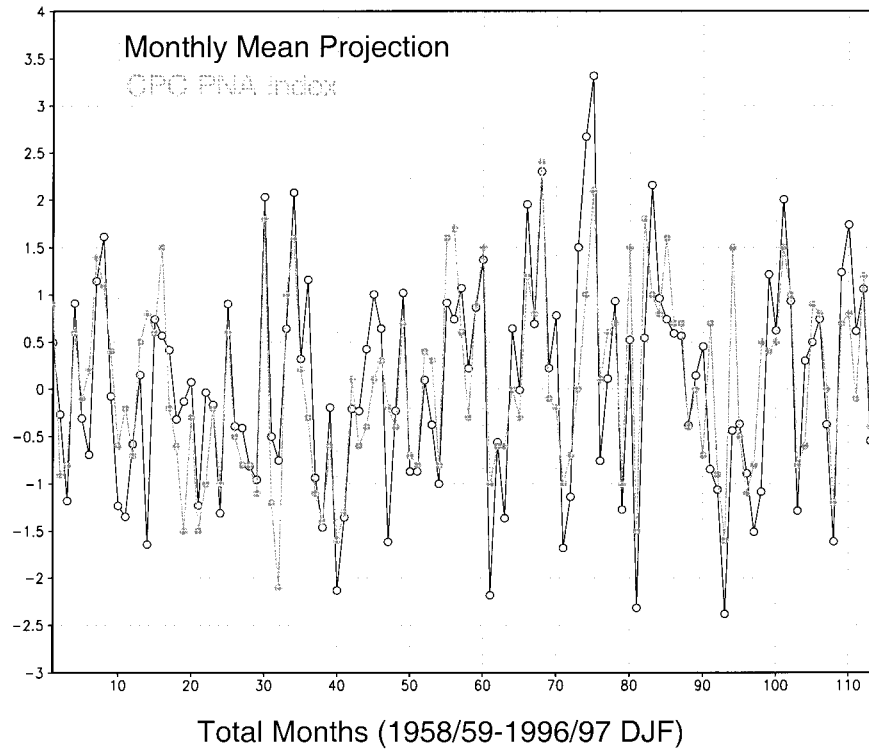


FIG. 4. CPC PNA index and monthly mean α . Closed circles are for the CPC PNA index and open circles are for the monthly mean $\alpha \times 10^{-8} \text{ m}^2 \text{ s}^{-1}$.

c. Tests of assumptions

The results presented in the previous sections are based on the assumption that (1) provides an accurate model for the system. However, it is well known that the atmosphere is *not* a purely linear system driven by a Gaussian white noise forcing. Thus, we must consider the extent to which our data fails to satisfy (1), and the related influence on our results.

A system that satisfies (1) exactly is subject to a number of constraints, which are described in detail in Penland and Sardeshmukh (1995). In brief, we find that the dataset represented by our choice of EOFs is nearly Gaussian, that the noise covariance matrix is positive-definite (all eigenvalues are positive), and that our system matrix \mathbf{B} shows only limited dependence on τ_o . In particular, the structure of the leading optimal for 5-day growth is robust under the choice of τ_o (not shown). For a pure linear Markov process, \mathbf{B} should be independent of τ_o (Gardiner 1985). However, as it is clear for our case that the atmosphere will not satisfy these criteria exactly, the most relevant test is simply how accurately (1) approximates the NH wintertime flow.

To test the assumptions, we first recalculate the covariance matrices in (3) from only the first 20 yr of the data. We then use these covariances in (2) and (3) to calculate the error variance as a function of prediction lead for the remaining years. Figure 8 compares the observed and expected growth in error variance, nor-

malized by the climatological variance. The expected growth in error variance arises from neglecting the stochastic forcing in (2), and takes the form

$$\langle \mathbf{e}(\tau) \mathbf{e}(\tau)^T \rangle = \mathbf{C}(0) - \mathbf{G}(\tau) \mathbf{C}(0) \mathbf{G}^T(\tau),$$

following Penland (1989), where $\mathbf{e}(\tau)$ is the error vector at lead τ . As expected, at longer lead times, the calculated error grows faster than the theoretical value, reflecting the influence of processes not represented in (1). However, the curves agree to within $\approx 20\%$ of the climatological variance at most leads, and to within 15% at 5 days, suggesting these neglected processes do not significantly degrade the ability of (1) to represent the system. The curves also demonstrate that even when the forcing is neglected the model exceeds the skill of a climatological prediction out to 12 days. Thus, Fig. 8 implies that our model of the system is reasonably robust despite the failings of (1), lending confidence to the derived results.

4. Summary and conclusions

In this study we investigate the ability of a linear stochastic model, derived from the observed data, to describe the evolution of atmospheric low-frequency flow. We find that optimal perturbations exist for a range of growth periods and retained EOFs, and further find that the leading optimal perturbation evolves into

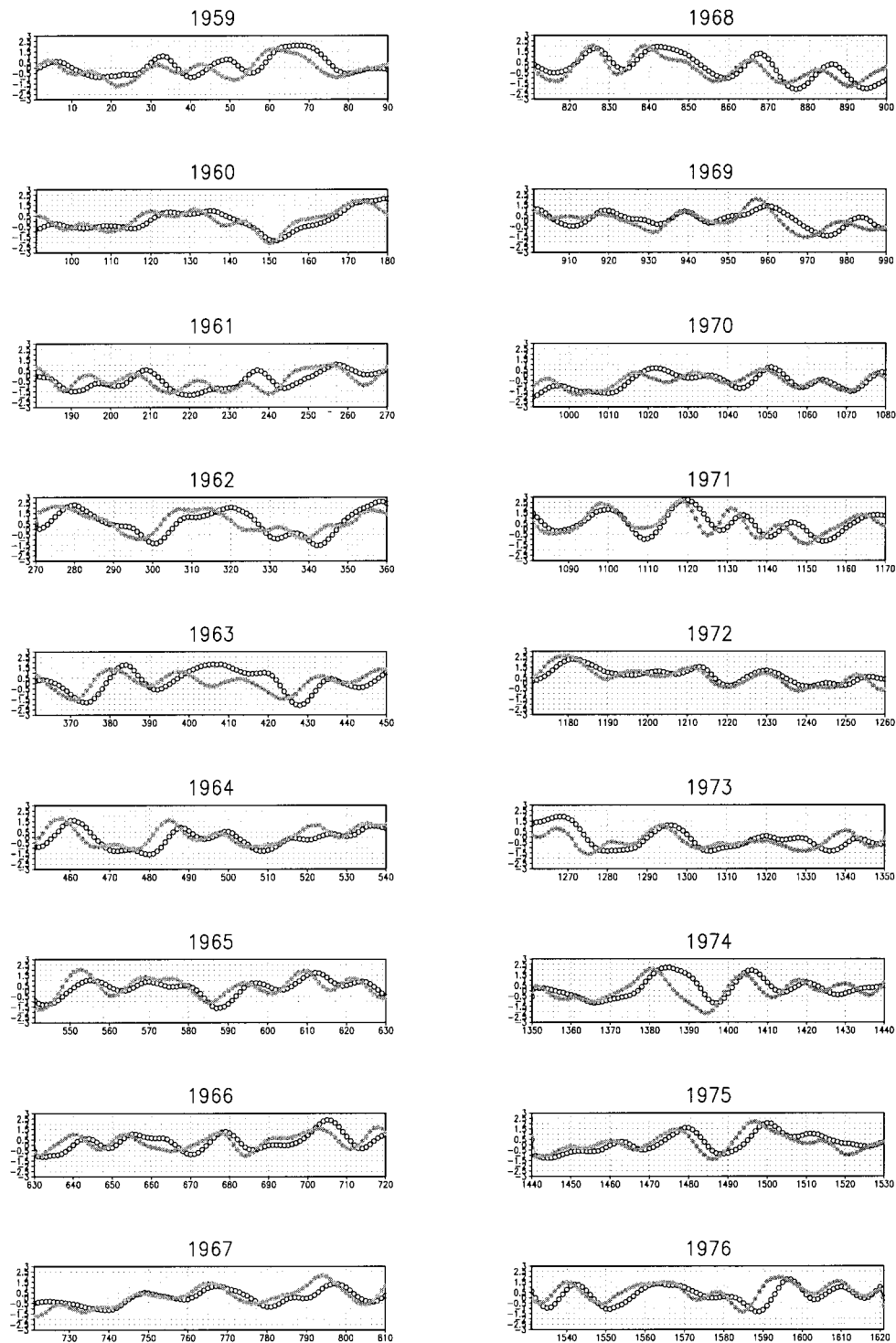


FIG. 5. The relationship between the PNA and the leading optimal. Open (closed) circles are for normalized α (β) for NH winter, 1958/59–1975/76. The x axis shows days of the winter seasons.

a pattern strongly resembling the PNA. The correlation between our PNA index based on this evolved pattern and the CPC index is high, confirming that this pattern is indeed the PNA. Also, the majority of PNA events

in the observed data are found to follow high projections onto the leading optimal. As all of the empirical normal modes (ENMs) are decaying, this result suggests that most of the PNA arises through optimal non-

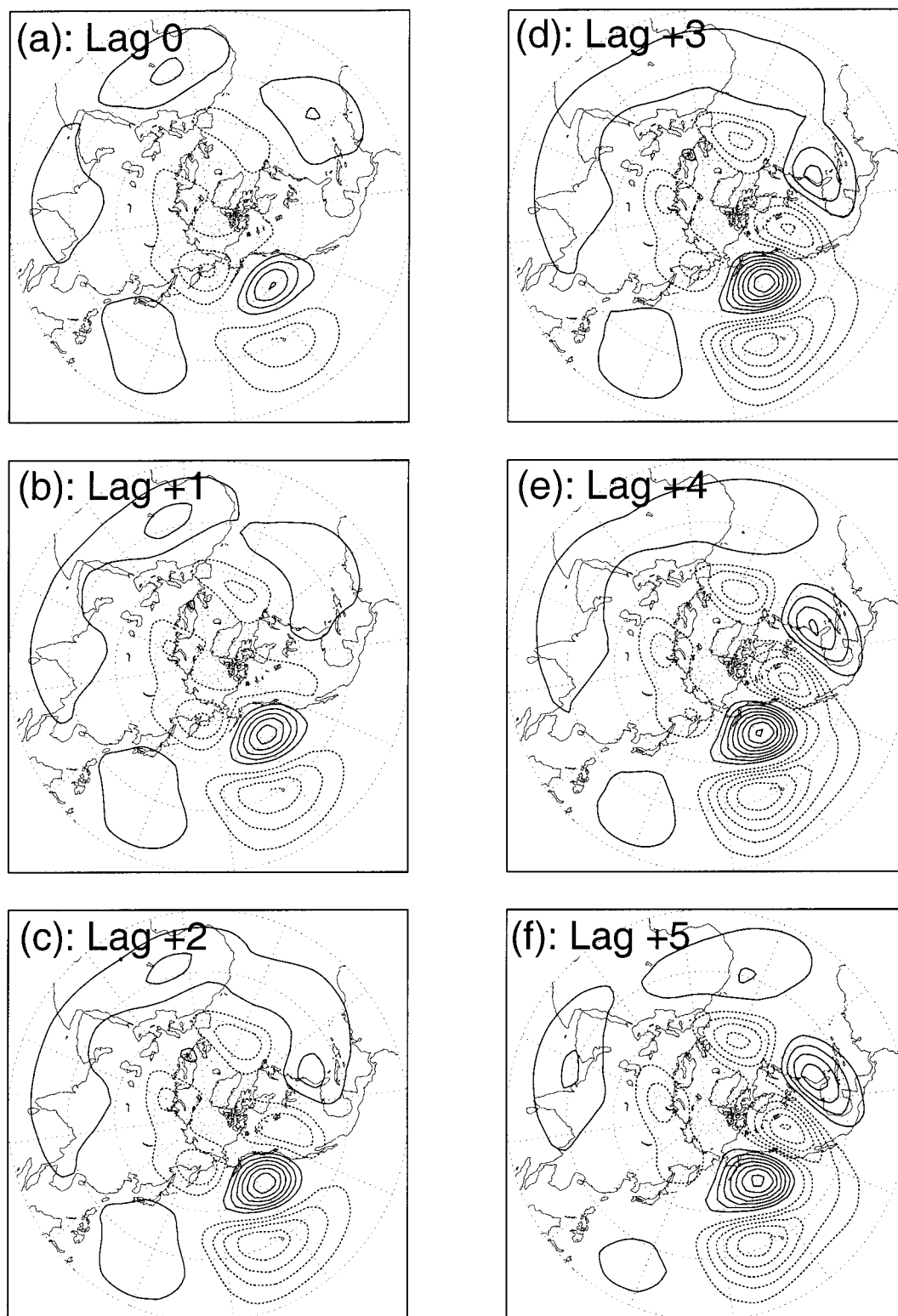


FIG. 6. Composite streamfunction anomaly at 300 mb from 60 negative phase PNA events for (a) lag 0, (b) lag +1, (c) lag +2, (d) lag +3, (e) lag +4, and (f) lag +5. Contour interval is $2 \times 10^6 \text{ m}^2 \text{ s}^{-1}$, solid contours are positive, dashed contours are negative, and the zero contour is omitted.

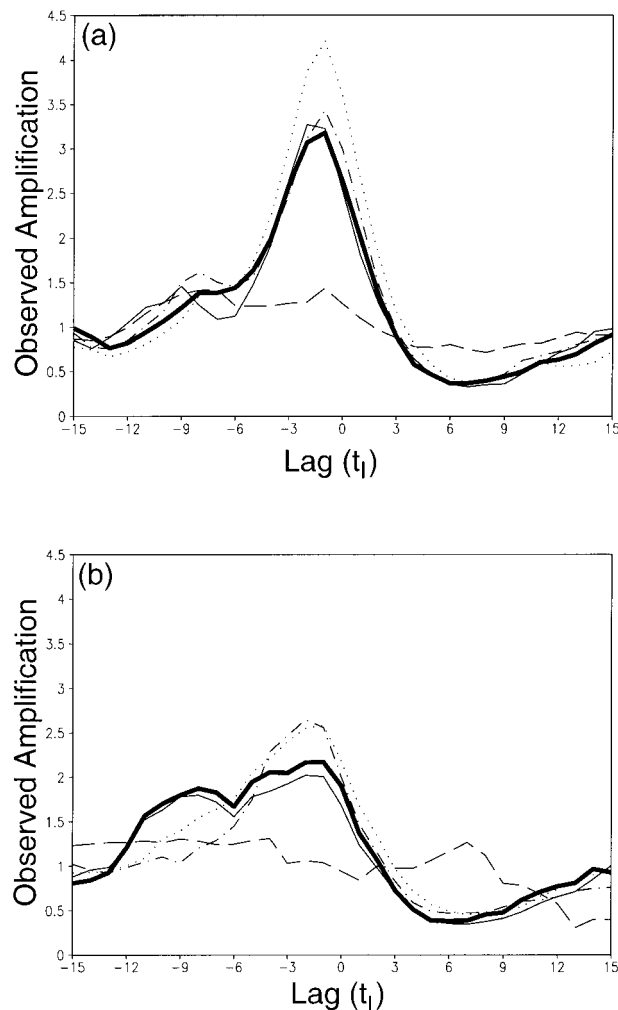


FIG. 7. Observed amplification of streamfunction variance for the (a) negative-phase PNA (60 events), and the (b) positive-phase PNA (57 events). The dotted line is for the 45 EOFs, the heavy solid line is for the 40 EOFs, the dashed-dotted line is for the 35 EOFs, the thin solid line is for the 30 EOFs, and the dashed line is for the 25 EOFs.

modal growth by constructive interference of decaying ENMs.

Comparison with previous studies provides some insight into the critical mechanisms captured by our linear operator. In particular, Newman et al. (1997, 1999, personal communication) suggest that stochastic models, constructed from either linear barotropic or linear balanced baroclinic models, cannot accurately reproduce the evolution of the observed low-frequency flow, such as the PNA. This then implies that the evolution of the PNA is strongly influenced by baroclinicity through divergence and/or aspects of nonlinear interactions that cannot be parameterized as a constant linear damping or white noise forcing. This result is consistent with Feldstein (1998), F2001, and Cash and Lee (2000), who find that nonlinear interactions between

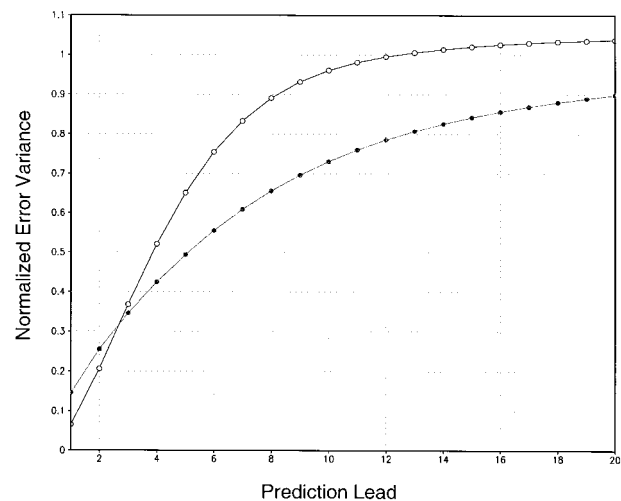


FIG. 8. Actual and theoretical growth in error variance. Open (closed) circles are for the observed (theoretical) error variance, normalized by the climatological variance as function of prediction lead time.

low-frequency waves and divergence play important roles in both the PNA and other low-frequency anomalies (LFAs) such as blocking, respectively. It should be noted that while divergence and nonlinearity appear to play crucial roles in governing the time-evolution of the PNA, this result is not necessarily inconsistent with the results of Simmons et al. (1983) noted in the introduction. Previous studies of the evolution of LFAs (Cash and Lee 2000; Feldstein 1998; and F2001) have shown that divergence and nonlinearity strongly influence the location of the anomalies, and act to retard downstream advection during the growth phase. In these studies, the growth of the anomaly results from linear barotropic interactions with the mean flow. By inhibiting downstream advection, divergence and nonlinear interactions allow the anomaly to spend more time in a favorable growth region. Thus, while not directly responsible for the growth process, they significantly influence the overall evolution of the anomaly pattern. It is also important to point out that our single-level stochastic model, which uses data at 300 mb only, also retains information on baroclinicity through divergence at that level. Given the capability of this stochastic model, the next natural step is to compare the empirically derived linear operator used here and the 300-mb linearized barotropic operator, to help us understand how the additional processes captured by the empirical operator act on the data.

The fact that our leading optimal (Figs. 2a–c) shows a baroclinic structure at lower latitudes over the tropical Pacific and an equivalent-barotropic character in the extratropics indicates that tropical convective heating may be important for triggering the PNA. In this scenario, a convective heating anomaly acts as a source for a poleward propagating Rossby wave, as suggested by the

work of Horel and Wallace (1981), and consistent with the results of F2001 and our picture described in the introduction. In order to substantiate this idea, a relationship between a more direct signature of tropical heating, such as outgoing longwave radiation, and the leading optimal needs to be sought. The structure of the leading optimal in the midlatitudes may be linked to another possible mechanism of PNA initiation. Dole and Black (1990) show that zonal wind anomalies over the central and eastern Pacific precede the onset of their persistent anomalies. The structure of the leading optimal in these regions is consistent with similar zonal wind anomalies (not shown). Preliminary results from a vorticity budget analysis suggest that the growth of the PNA is dependent on the location and configuration of the leading optimal relative to the stationary waves, and may be less sensitive to the generation mechanism. It may be that both tropical convection and midlatitude dynamics can play a role in PNA onset. F2001 also finds that PNA onset resembles an initial value problem, further supporting this hypothesis.

The results presented here also hold implications for the PNA timescale. Both the MA curve and the composites indicate a PNA timescale of ≈ 10 days. This scale is consistent with F2001, who examines the time evolution of the PNA in detail, and with Dole and Black (1990). However, most studies have examined the PNA through the use of monthly mean or seasonal statistics, making direct comparison with the current study difficult. Given that the PNA pattern represents the maximum growth in ψ' variance, it is not surprising that it plays a prominent role in the monthly mean statistics. However, with a timescale of 10 days, a monthly mean may involve averaging over several events, and possibly obscure important details of PNA development. In particular, our results require that a plausible PNA onset mechanism be able to operate over a period of a few days. Recalling that the Fourier transform of the delta function is white in frequency space, from an idealized perspective, this short-onset timescale is consistent with the assumption of white noise forcing in the linear-stochastic model.

One method for investigating the PNA onset problem in more depth involves examination of the ENMs. While there are a number of difficulties in the physical interpretation of ENMs for a nonlinear data set (Penland 1989; Penland and Ghil 1993; Zhang et al. 1997) due to degeneracy of the modes, we have found several ENMs whose spatial patterns and periods are robust between single and multilevel calculations and over a range of EOF truncations. It is hoped that examination of these ENMs and their adjoints will lead to additional insight into the onset and decay mechanisms captured by our linear operator, and thus to a deeper understanding of the observed PNA evolution.

Acknowledgments. This manuscript greatly benefitted from conversations with Dr. Steven Feldstein, and the

comments of two anonymous reviewers. Thanks are due to Dr. Cecile Penland for helping us in the calculation of the ENMs. We would also like to thank the NOAA Climate Diagnostic Center for providing us with the NCEP–NCAR reanalysis dataset. This research was supported by the National Science Foundation through Grant ATM-9712824.

REFERENCES

- Barnston, A. G., and R. E. Livezey, 1987: Classification, seasonality, and persistence of low-frequency atmospheric circulation patterns. *Mon. Wea. Rev.*, **115**, 1083–1126.
- Branstator, G., 1992: The maintenance of low-frequency atmospheric anomalies. *J. Atmos. Sci.*, **49**, 1924–1945.
- , 1995: Organization of storm track anomalies by recurring low-frequency circulation anomalies. *J. Atmos. Sci.*, **52**, 207–226.
- Cash, B. A., and S. Lee, 2000: Dynamical processes of block evolution. *J. Atmos. Sci.*, **57**, 3202–3218.
- Dole, R. M., and R. X. Black, 1990: Life cycles of persistent anomalies. Part II: The development of persistent negative height anomalies over the north Pacific Ocean. *Mon. Wea. Rev.*, **118**, 824–846.
- Feldstein, S., 1998: The growth and decay of low-frequency anomalies in a GCM. *J. Atmos. Sci.*, **55**, 415–428.
- Frederiksen, J. S., 1983: A unified three-dimensional instability theory of the onset of blocking and cyclogenesis. II: Teleconnection patterns. *J. Atmos. Sci.*, **40**, 2593–2609.
- , and P. J. Webster, 1988: Alternative theories of atmospheric teleconnections and low-frequency fluctuations. *Rev. Geophys.*, **26**, 459–494.
- Gardiner, C. W., 1985: *Handbook of Stochastic Methods for Physics, Chemistry, and the Natural Sciences*. Springer-Verlag, 442 pp.
- Hasselmann, K., 1988: PIPs and POPs: The reduction of complex dynamical systems using principal interaction and oscillation patterns. *J. Geophys. Res.*, **93**, 11 015–11 021.
- Horel, J. D., and J. M. Wallace, 1981: Planetary scale atmospheric phenomena associated with the Southern Oscillation. *Mon. Wea. Rev.*, **109**, 813–829.
- Hoskins, B. J., and D. J. Karoly, 1981: The steady linear response of a spherical atmosphere to thermal and orographic forcing. *J. Atmos. Sci.*, **38**, 1179–1196.
- Kalnay, E., and Coauthors, 1996: The NCEP/NCAR 40-Year Reanalysis Project. *Bull. Amer. Meteor. Soc.*, **77**, 437–471.
- Lau, N.-C., 1981: A diagnostic study of recurrent meteorological anomalies appearing in a 15-year simulation with a GFDL general circulation model. *Mon. Wea. Rev.*, **109**, 2287–2311.
- , 1988: Variability of the observed midlatitude stormtracks in relation to low-frequency changes in the circulation pattern. *J. Atmos. Sci.*, **45**, 2718–2743.
- Newman, M., P. D. Sardeshmukh, and C. Penland, 1997: Stochastic forcing of the wintertime extratropical flow. *J. Atmos. Sci.*, **54**, 435–455.
- Penland, C., 1989: Random forcing and forecasting using principal oscillation pattern analysis. *Mon. Wea. Rev.*, **117**, 2165–2185.
- , and M. Ghil, 1993: Forecasting Northern Hemisphere 700-mb geopotential height anomalies using empirical normal modes. *Mon. Wea. Rev.*, **121**, 2355–2372.
- , and P. D. Sardeshmukh, 1995: The optimal growth of tropical seas surface temperature anomalies. *J. Climate*, **8**, 1999–2024.
- Sardeshmukh, P. D., M. Newman, and M. D. Borges, 1997: Free barotropic Rossby wave dynamics of the wintertime low-frequency flow. *J. Atmos. Sci.*, **54**, 5–23.
- Simmons, A. J., J. M. Wallace, and G. W. Branstator, 1983: Barotropic wave propagation and instability, and atmospheric teleconnection patterns. *J. Atmos. Sci.*, **40**, 1363–1392.

- Ting, M., and N.-C. Lau, 1993: A diagnostic and modeling study of the monthly mean wintertime anomalies appearing in a 100-year GCM experiment. *J. Atmos. Sci.*, **50**, 2845–2867.
- Wallace, J. M., and D. S. Gutzler, 1981: Teleconnections in the geopotential height field during the norther hemisphere winter. *Mon. Wea. Rev.*, **109**, 784–812.
- Webster, P. J., 1981: Mechanisms determining the atmospheric response to sea surface temperature anomalies. *J. Atmos. Sci.*, **38**, 554–571.
- Zhang, Y., V. Dymnikov, and J. M. Wallace, 1997: Sensitivity test of POP system matrices—an application of spectral portrait of a nonsymmetric matrix. *J. Climate*, **10**, 1753–1758.